International Forum on Aeroelasticity and Structural Dynamics
IFASD 2024
17-21 June 2024, The Hague, The Netherlands

NUMERICAL ANALYSIS OF THE UNSTEADY WING-TAILPLANE INTERACTION IN TWO-DIMENSIONAL FLOWS

Kristopher Davies[1] **and Michael Fehrs**[1]

[1]German Aerospace Center (DLR)
Bunsenstr. 10, 37073 Göttingen
kristopher-marc.davies@dlr.de, michael.fehrs@dlr.de

Keywords: CFD, unsteady aerodynamics, buffet, stall, turbulent flows

Abstract: This article presents a study of the horizontal tailplane (HTP) buffet phenomenon, which is caused by a highly unsteady inflow of the HTP. The configuration of the wing and HTP is derived from the NASA Common Research Model. Steady results are presented which serve as a prerequisite to identify potential flow conditions in terms of HTP buffet. Subsequently, unsteady results are presented for selected low speed and high speed cases, for which the interaction between the wing and HTP are discussed. For both flow speeds, a periodic fluctuation of the lift coefficient is observed on the main wing and HTP with a dominant low frequency oscillation. For the low speed case, this oscillation is related to an unsteadiness as a result of severe separation on the upper side of the main wing, whereas the low frequent oscillation of the high speed case is attributed to transonic shock buffet on the main wing. For both cases, these mechanisms also dominate the fluctuations on the HTP segment, which is additionally influenced by high frequent oscillation as a result of vortex shedding. The latter is increasingly dominating at high angles of attack.

1 INTRODUCTION

The buffet phenomenon is commonly associated to the self-induced unsteady motion of a shock as a result of an interaction with the separated boundary layer on a wing in transonic conditions (*transonic shock buffet*). Another unsteady flow phenomenon linked to separated flows is the so-called *horizontal tailplane (HTP) buffet*. Contrary to shock buffet, HTP buffet is an externally induced unsteadiness as it is the consequence of turbulent structures convecting from the separated wing to the tailplane. These turbulent structures lead to fluctuations of the pressure distribution (buffet) and structural vibrations (buffeting) of the HTP [1]. The dominating flow mechanisms and the critical frequency range causing HTP buffet are insufficiently understood.

While comparatively high attention has been paid to the transonic shock buffet phenomenon, less publications exist with regard to tail buffet. For the latter, the majority refers to military configurations, as the occurrence of tail buffet is likely due to the specific flow features on such aircraft. These involve high angles of attack with large vortex structures being generated by the leading edge extensions (LEX). These vortices can potentially burst or breakdown as a result of disturbances and unsteadiness, eventually causing high dynamic loads and structural vibrations on the tailplanes [2].

Nevertheless, HTP buffet on civil transport aircraft gains more importance in recent experimental [1] and numerical [3, 4] investigations. In particular, the unsteady wing-tailplane interaction is addressed within the research unit FOR 2895 (Unsteady flow and interaction phenomena at

high-speed stall conditions) of the German Research Foundation by means of wind tunnel tests and numerical studies [5].

The present study aims to contribute to a better understanding of the HTP buffet phenomenon. For this purpose, the unsteady wing-tailplane interaction is analysed for a 2D configuration in stall conditions based on unsteady RANS simulations using a Reynolds stress turbulence model. Based on previous analysis of wake flows with severe separation [6], this model is considered as suitable for the subsequent study. The stall conditions are initially identified by steady computations for a variation of the Mach number and angle of attack. Unsteady computations are subsequently performed for the stall region of each Mach number and potential critical flow conditions are identified with respect to HTP buffet. Eventually, the unsteady wing-tailplane interaction is investigated in more detail for selected low speed and high speed cases.

2 METHOD AND NUMERICAL SETUP

2.1 Airfoil Selection

In order to obtain a realistic wing-tailplane configuration, consisting of representative airfoils for the wing and HTP of a civil transport aircraft, the NASA Common Research Model [7, 8] is consulted. This model provides a suitable basis, as it represents a state-of-the-art civil aircraft model operating at transonic speeds with a lift coefficient of $C_L = 0.5$ at a design cruise Mach number of $M = 0.85$ and a Reynolds number of $Re = 40 \cdot 10^6$.

Since it is desired to derive a 2D model of the 3D Common Research Model, an appropriate spanwise position initially needs to be identified, along which the airfoils of the wing and HTP are extracted subsequently. The area of interest is therefore limited to the inboard region of the wing up to the spanwise position of the HTP tip. The cutting position should ideally not be affected by 3D effects, i.e. interference of the fuselage.

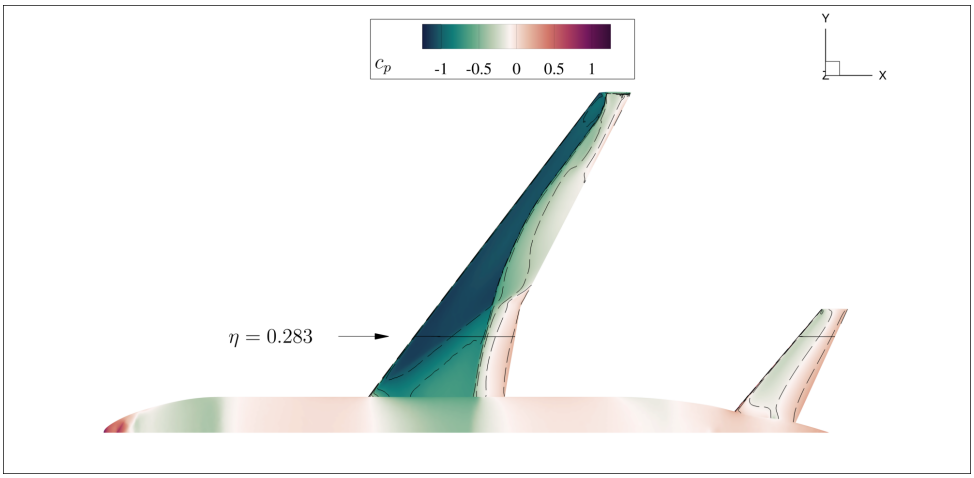

Figure 1: Selection of a cutting position on the NASA Common Research Model for a 2D wing-HTP configuration

Fig. 1 presents results of a preliminary CFD computation for the 3D Common Research Model at a Mach number of $M = 0.85$ and an angle of attack $\alpha = 4.0°$. The latter is chosen to ensure a certain robustness for the selected cutting position, as flow separation is more likely at higher angles of attack. The dashed lines on the contour plot indicate isobars. A suitable cutting position is found where the isobars are deflected only sparsely. Based on these findings, a cutting position is selected at the spanwise position $\eta = 0.283$, as indicated by the solid line in Fig. 1.

As the extracted sections of the wing and HTP airfoils are designed for a swept wing and HTP, respectively, the effect of the sweep angles need to be corrected for 2D flows. This transformation is approximated through the concept of an infinite swept wing [10, 11]:

$$\left(\frac{t}{c}\right)_{2D} = \frac{\left(\frac{t}{c}\right)_{3D}}{cos(\varphi_{LE})} \tag{1}$$

Where φ_{LE} is the leading edge sweep angle of the wing and HTP, respectively. In case of the Common Research Model, the corresponding angles are $\varphi_{LE,Wing} = 35°$ and $\varphi_{LE,HTP} = 37.5°$. Following Eq. 1, the relative thicknesses of the airfoils are thus increased in the 2D case compared to the 3D case.

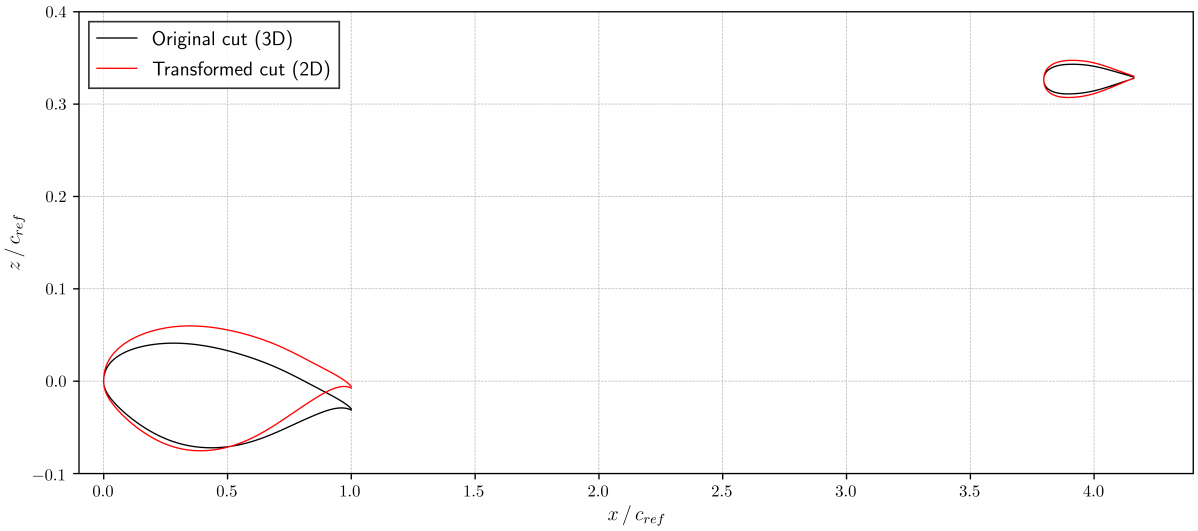

Figure 2: Comparison of the original (3D) and transformed (2D) airfoils of the wing and HTP at $\eta = 0.283$

The resulting 2D airfoils for the wing and HTP are presented in Fig. 2. It should be noted that the twist angles of the 3D airfoils are rotated to zero degrees for the 2D airfoils. Additionally, the chord lengths are scaled to a reference length of $c_{ref} = 1$ m with respect to the wing section.

2.2 Numerical Grid

The computational grid is generated using the commercial software CENTAUR™ [9]. The upper and lower side of the airfoils are each discretised with 400 grid points for the wing and 200 grid points for the HTP section, resulting in a spacing of $\Delta x/c \approx 0.002$. The boundary layer consists of 95 structured layers with a normal growth rate of 1.1. This setup allows y^+ values of $y^+ < 1$ for all investigated cases.

The wing and HTP airfoils are connected with a structured mesh, consisting of a nominal spacing $\Delta x/c_{ref} \approx 0.02$, with c_{ref} being the reference length of the wing section. The overall grid consists of approximately $6.2 \cdot 10^5$ grid points. Fig. 3 presents the surrounding mesh of the wing and HTP sections.

2.3 Flow Conditions

Similar to the geometrical correction highlighted in Sec. 2.1, the flow conditions of the 3D configuration need to be corrected to ensure consistency. Accordingly, the Mach number and

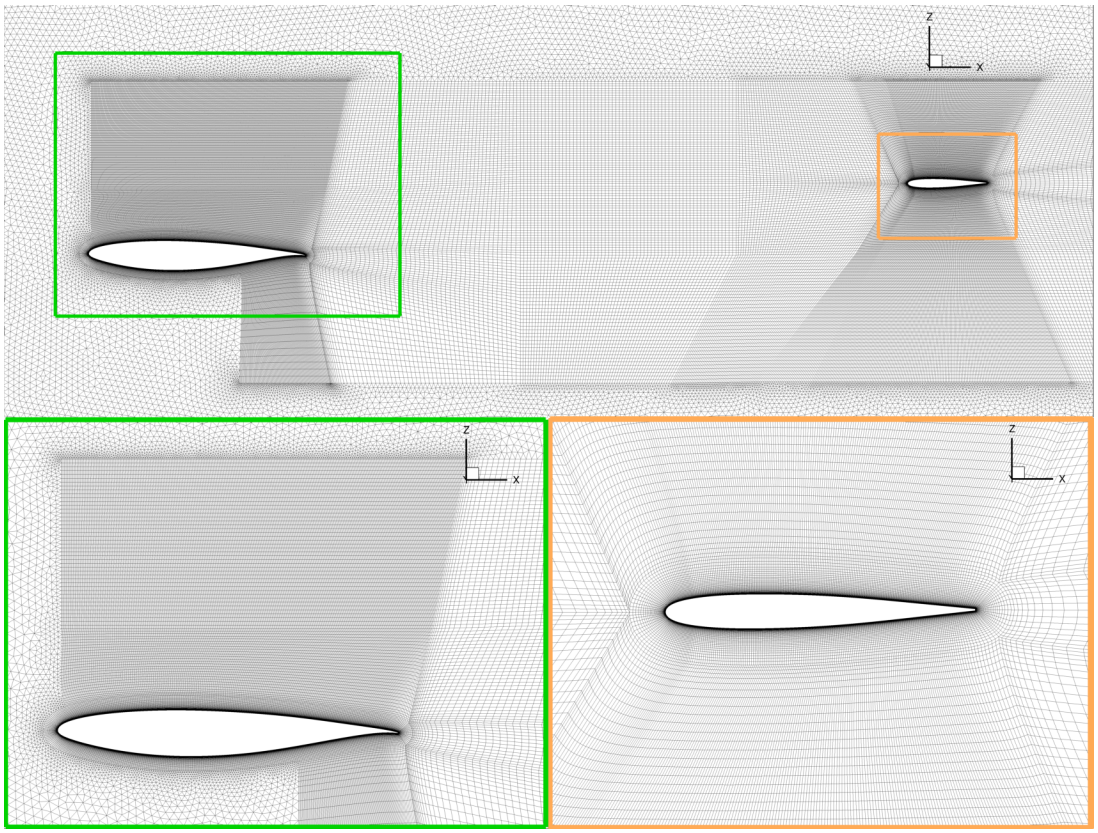

Figure 3: Numerical grid with closeup views of the wing and HTP surroundings

Reynolds number for 2D flows are considered as [10, 11]:

$$M_{2D} = M_{3D} \cdot cos(\varphi_{LE}) \tag{2}$$

$$Re_{2D} = Re_{3D} \cdot cos^2(\varphi_{LE}) \tag{3}$$

It should be noted that Eq. 2 and 3 are calculated for the leading edge sweep angle of $\varphi_{LE,Wing} = 35°$ only.

The 2D simulations are performed for a variation of the Mach number, while the Reynolds number is held constant at $Re_{3D} = 30 \cdot 10^6$. Two different Mach numbers are selected, where the first is chosen representative for moderate transonic effects and the second with distinct transonic effects. The resulting 2D flow conditions (following Eq. 2 and 3) are listed in Table 1:

Table 1: Flow parameters for the 2D simulations

M_{3D}	M_{2D}	Re_{3D}	Re_{2D}
0.85	0.6963	$30 \cdot 10^6$	$20.13 \cdot 10^6$
0.40	0.3277	$30 \cdot 10^6$	$20.13 \cdot 10^6$

Subsequently, the case at $M = 0.3277$ is referred to as *low speed* case and $M = 0.6963$ as *high speed* case.

2.4 Flow Solver and Setup

The flow simulations within this study are performed with the DLR TAU-Code [12]. The convective flux discretisation is realised using a second order central scheme with artificial matrix dissipation. A second-order Roe upwind scheme is applied for the discretisation of the convective fluxes of the turbulence equation. Temporal discretisation is realised using an implicit Backward-Euler method, where the linear system is solved with an LU-SGS scheme [13]. The dual-time-stepping algorithm of Jameson [14] is applied for unsteady computations. For each variation of the Mach number, a physical time step is chosen in the range of 0.1-1% of the convective time scale u_∞/c_{ref}, resulting in a range of $9 \cdot 10^{-6} \leq \Delta t/s \leq 3 \cdot 10^{-5}$. The number of inner iterations are $n_{inner} = 500$.

The SSG/LRR-ω Reynolds stress model [15] is applied throughout this study. This turbulence model combines the pressure-strain model by Speziale, Sarkar and Gatski (SSG) [16] and Launder, Reece and Rodi (LRR) [17] in the near-wall region. The length scale is supplied through the baseline ω-equation by Menter [18]. The applied version of the SSG/LRR-ω uses a logarithmic transformation of the length scale ω for improving the numerical robustness [19].

3 RESULTS

3.1 Steady Results

In order to identify potential critical flow conditions in terms of HTP buffet, steady computations are initially performed for a range of the angle of attack and each Mach number listed in Tab. 1. The resulting overall lift coefficients, consisting of the wing and HTP components, are presented in Fig. 4 with its mean and standard deviations of the last 5000 iterations.

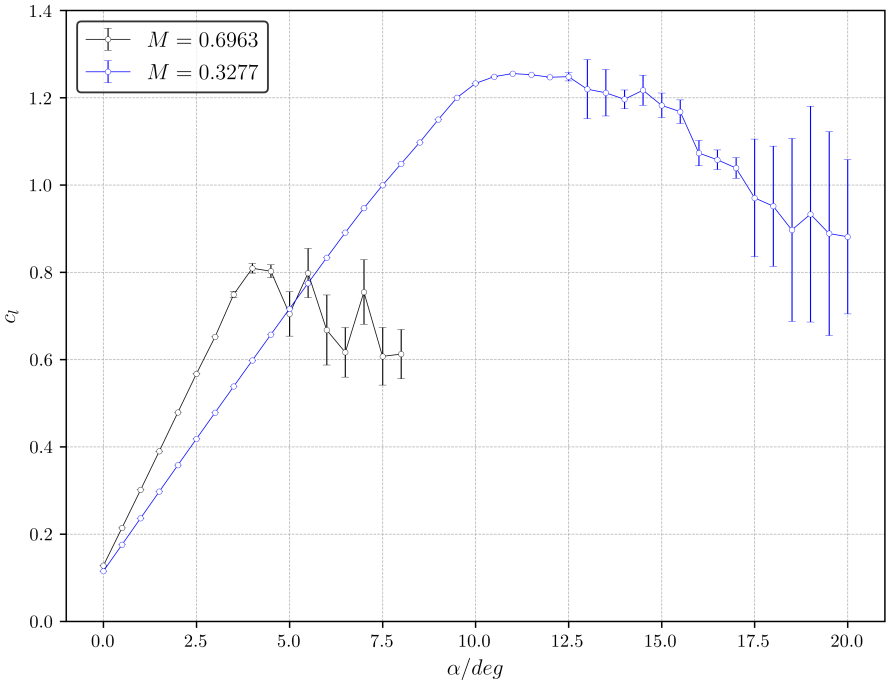

Figure 4: Steady polar for a variation of the Mach number

At $M = 0.6963$, the maximum lift coefficient is reached in the range of $4.0° \leq \alpha \leq 4.5°$, where first significant deflections can be observed. These deflections increase for the angles of attack in the stall region, indicating the presence of unsteady flows.

For the low speed case at $M = 0.3227$, the maximum lift coefficient is reached at $\alpha \approx 11.0°$.

First fluctuations of the lift coefficient are present for $\alpha \geq 12.5°$, with the largest fluctuations in the deep stall region at $\alpha \geq 17.5°$.

3.2 Unsteady Results

3.2.1 Low Speed

The wing-tailplane interaction is initially analysed for low speed conditions at $M = 0.3277$. In order to identify the case with first oscillations on the HTP (i.e. buffet), unsteady simulations are performed in the stall region beyond $\alpha \geq 11.0°$. Fig. 5 shows the development of the lift coefficient time series of the wing and HTP components for a variation of the angle of attack, respectively. The time is expressed as the dimensionless convective time scale unit $t_{conv} = t \cdot u_\infty / c_{ref}$. As can be clearly seen here, first significant oscillations are present at $\alpha = 12.5°$ for both, the wing and HTP components. This case is analysed in more detail, subsequently.

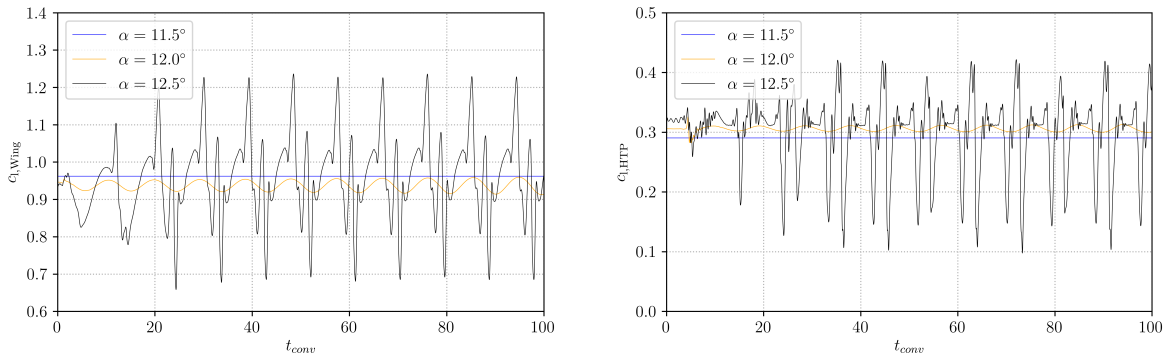

(a) Wing (b) HTP

Figure 5: Lift coefficient time series for the wing (left) and HTP (right) components for a variation of the angle of attack at $M = 0.3277$

Fig. 6 and 7 show the lift coefficient time series and power spectral densities for the wing and HTP, respectively. Only a part of the time series is shown for clarity purposes. The power spectral densities are computed using Welch's method [20] and refer to the frequency and Strouhal number, where the latter is defined as $Sr = f \cdot c_{ref} / u_\infty$. The time series of the wing shows a periodic signal with a corresponding dominant frequency at $f = 11.9$ Hz, or a Strouhal number of $Sr = 0.11$. This frequency is in agreement to a low frequency oscillation reported by Zaman et al. [21] for a different airfoil at stall onset conditions. The authors refer the Strouhal number with respect to the projected airfoil height d perpendicular to the freestream instead of the chord length c_{ref}, i.e. $Sr_d = f \cdot c_{ref} \cdot sin(\alpha) / u_\infty$, as a function of the angle of attack α. The reported oscillation has a frequency of $Sr_d \approx 0.02$. In case of the low frequency peak shown in Fig. 6 and 7 of $f = 11.9$ Hz, this leads to $Sr_d = 0.024$. Broeren and Bragg [22] experimentally investigated the stall behaviour for different airfoils, revealing that such severe fluctuations of the lift coefficient are associated to airfoils with a combination of thin airfoil and trailing edge stall types. They suggest that this unsteadiness is caused by an interaction of the leading edge and trailing edge separation bubbles [22]. Their reported frequencies for different airfoils and angles of attack lie in a range of $0.01 < Sr_d < 0.03$, which is indicated by the area filled in blue of Fig. 6 and 7. Furthermore, the fluctuations of the lift coefficient for a combination of thin airfoil and trailing edge stall types reported by Broeren and Bragg [22] are in agreement to the present case ($c_{l,rms,Wing} = 0.1122$).

The region filled in red of Fig. 6 and 7 corresponds to characteristic vortex shedding frequencies following Huang and Lin [24]. The authors observed that the vortex shedding frequency is depending on the angle of attack and Reynolds number for sufficiently low angles of attack.

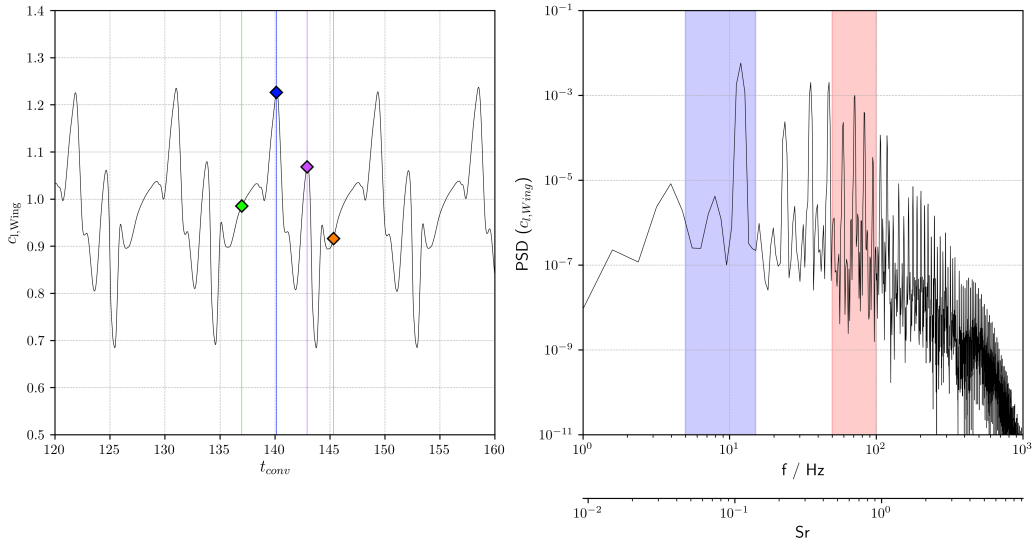

Figure 6: Time signal of the lift coefficient (left) and power spectral densities (right) of the wing section at $M = 0.3277$ and $\alpha = 12.5°$

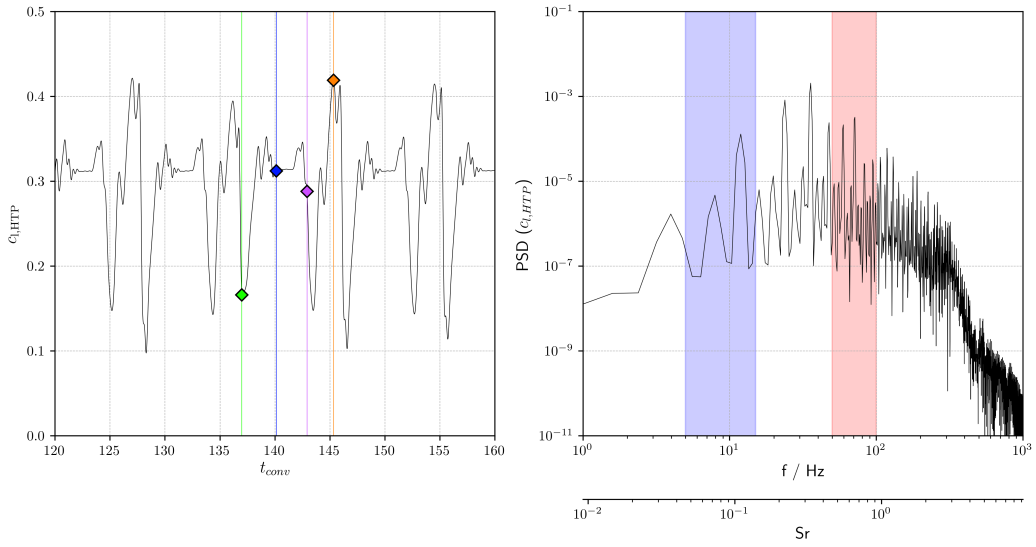

Figure 7: Time signal of the lift coefficient (left) and power spectral densities (right) of the HTP section $M = 0.3277$ and $\alpha = 12.5°$

For high angles of attack, the shedding frequency becomes constant for increasing Reynolds numbers, resulting in frequencies of $0.12 < Sr_d < 0.22$ for a variation of the angle of attack. In the present case, however, the frequency peaks within this range are rather associated to the higher harmonics of the low frequent oscillation at $f = 11.9$ Hz.

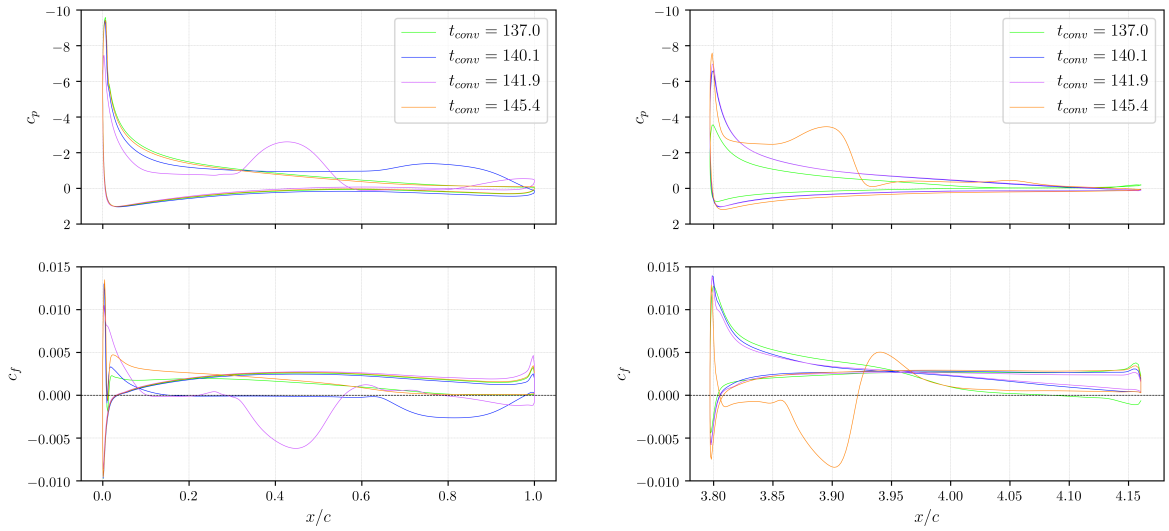

(a) Wing (b) HTP

Figure 8: Instantaneous pressure and skin friction distributions on the wing and HTP sections at $M = 0.3277$ and $\alpha = 12.5°$

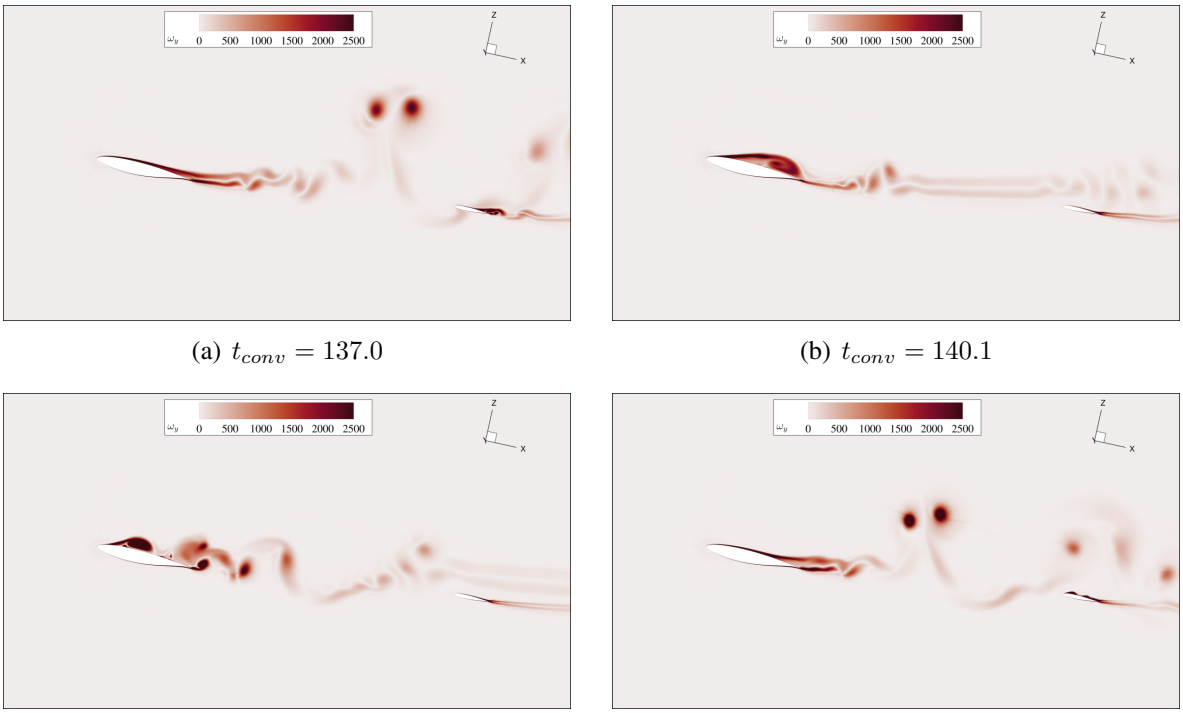

(a) $t_{conv} = 137.0$ (b) $t_{conv} = 140.1$

(c) $t_{conv} = 141.9$ (d) $t_{conv} = 145.4$

Figure 9: Instantaneous vorticity at $M = 0.3277$ and $\alpha = 12.5°$

The coloured symbols in the time series of Fig. 6 and 7 mark specific times, for which the instantaneous flow features are subsequently discussed in more detail. For this purpose, the corresponding pressure and skin friction distributions (Fig. 8), as well as the vorticity field (Fig. 9) are consulted.

At the first snapshot (green symbol, $t_{conv} = 137.0$), a strong suction peak is present near the leading edge of the upper wing section. A short region of boundary layer separation can be recognised downstream of the suction peak. Further downstream, the boundary layer remains attached and the shear layer is concentrated to the region close to the airfoil. At the same time, the HTP section is impinged by a vortical structure, causing a significant breakdown of the suction peak on the suction side of the HTP section. At the time where the maximum lift coefficient is reached at the wing section (blue symbol, $t_{conv} = 140.1$), the shear layer is widely extended and a clockwise rotating structure appears above the upper side. This vortical structure produces an additional suction effect on the upper wing side, as suggested in the corresponding pressure distribution. Subsequently, the shear layer becomes unstable and a vortex shedding process is initiated due to an interaction with the shear layer of the lower side. The latter produces counter-clockwise rotating vortices, which convect into the wake and partially impinge on the HTP section. However, a majority of structures with high vorticity convect above the HTP section (see Fig. 9 (d)). The last snapshot refers to the time where the maximum lift coefficient is reached on the HTP section (orange symbol, $t_{conv} = 145.4$). At this stage, the shear layer on the upper side of the HTP thickens and rolls up, which produces a significant suction effect as shown in the corresponding pressure distribution. However, this structure is only present for a substantial short period of time, as it convects downstream. Additionally, a vortical structure generated in the wake of the wing section is impinging on the HTP, which causes another lift breakdown similar to the first snapshot.

In order to compare the wing-tailplane interaction for a case in deep stall conditions, the angle of attack $\alpha = 19.0°$ is consulted. The time history of the lift coefficient and the corresponding power spectral densities for the wing and HTP components are shown in Fig. 10 and 11. Compared to the time signals at $\alpha = 12.5°$ (see Fig. 6 and 7), the signal appears less periodic with higher frequency oscillations. A corresponding peak can be identified at a frequency of $f \approx 60$ Hz, which corresponds to $Sr_d = 0.18$. Accordingly, this frequency is located well within the range of bluff body vortex shedding following Huang and Lin [24]. It is worth to note that the lift fluctuations are decreased at the wing component as compared to $\alpha = 12.5°$. However, the opposite is the case for the HTP component, as the fluctuations significantly increase at $\alpha = 19.0°$ compared to $\alpha = 12.5°$ (see Tab. 2).

Table 2: Fluctuations of the lift coefficient for low speed stall onset and deep stall conditions

α	$c_{l,rms,Wing}$	$c_{l,rms,HTP}$
12.5	0.1122	0.0644
19.0	0.0787	0.1318

This trend may be indicated through the instantaneous vorticity presented in Fig. 12 (a). The shear layer of the upper wing side is already in an unstable state shortly downstream of the leading edge, with a vortex street being developed in the wake as a result of an interaction with the shear layer of the lower side. In the process, the unstable shear layer of the upper side is limited to a region with a certain distance from the airfoil surface. This state is retained throughout the time, suggesting that the fluctuations are concentrated to the wake rather than the upper wing side. In turn, the wake is dominated by coherent structures of high vorticity.

Due to the high incidence, the vortical structures appear not to impinge on the HTP section, but a similar unsteadiness is present on the HTP section as for the wing component. Compared to the wing section, a shear layer is established, which causes fluctuations on the upper side of the HTP section and may explain the higher values of $c_{l,rms}$. Although the HTP section seems not to be directly impinged by the vortices in the wake of the wing, the inflow on the HTP section is disturbed by these structures as shown by the instantaneous Mach number presented in Fig. 12 (b). This presumably leads to additional high fluctuations on the HTP.

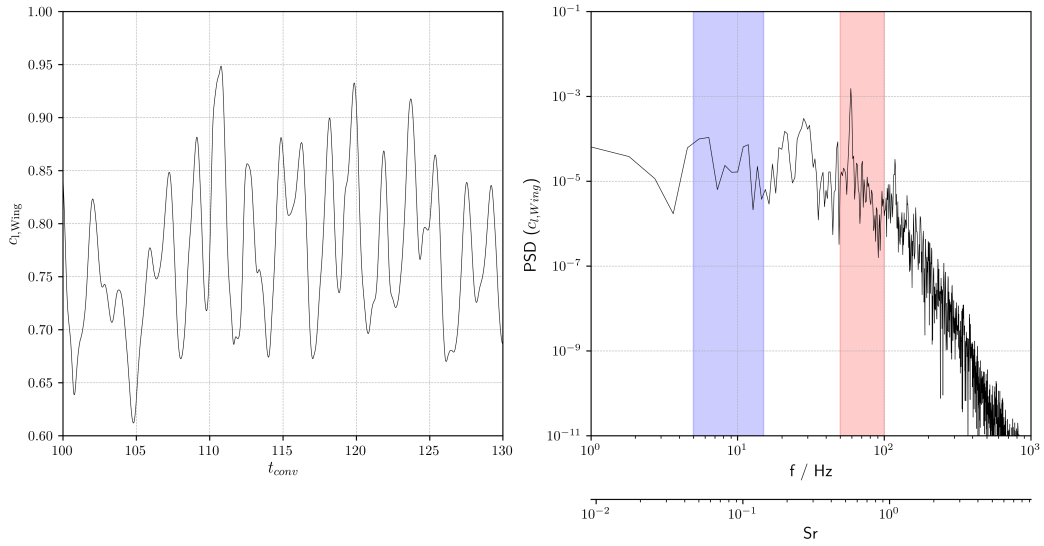

Figure 10: Time signal of the lift coefficient (left) and power spectral densities (right) of the wing section at $M = 0.3277$ and $\alpha = 19.0°$

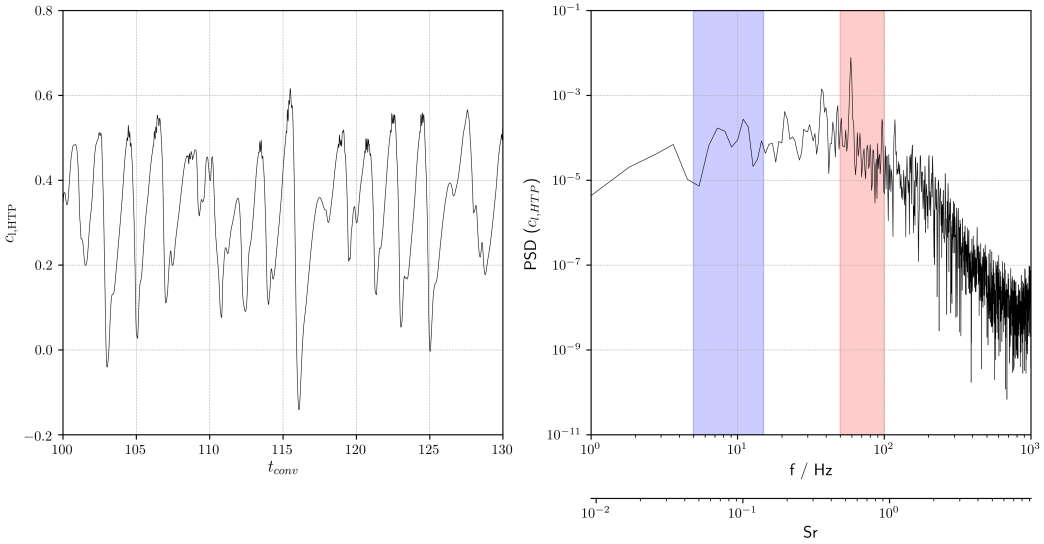

Figure 11: Time signal of the lift coefficient (left) and power spectral densities (right) of the HTP section at $M = 0.3277$ and $\alpha = 19.0°$

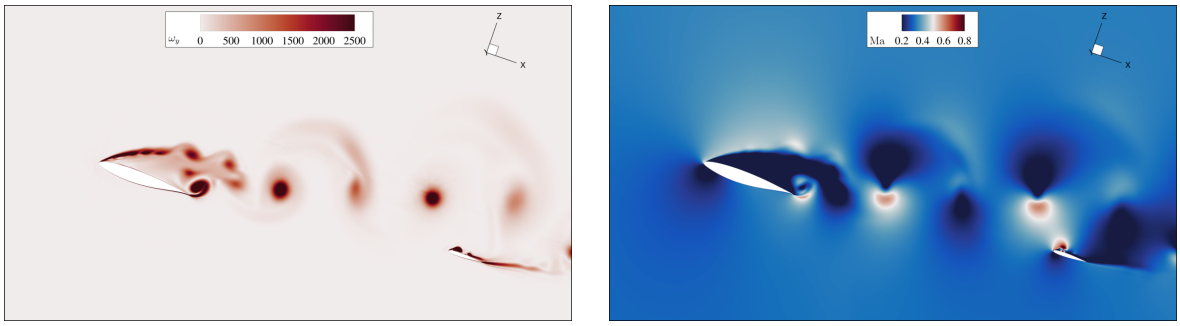

(a) Vorticity (b) Mach number

Figure 12: Instantaneous vorticity at $M = 0.3277$ and $\alpha = 19.0°$

3.2.2 High Speed

The previous analysis is analogically performed for high speed conditions at $M = 0.6963$. As suggested by the steady polar (see Fig. 4), the maximum lift coefficient is reached in the proximity of $\alpha \approx 4.0°$. Accordingly, unsteady simulations are performed for $\alpha \geq 4.0°$. The time series of the wing and HTP lift coefficients presented in Fig. 13 clearly show a buffet onset condition at $\alpha = 5.0°$. This case is analysed in more detail.

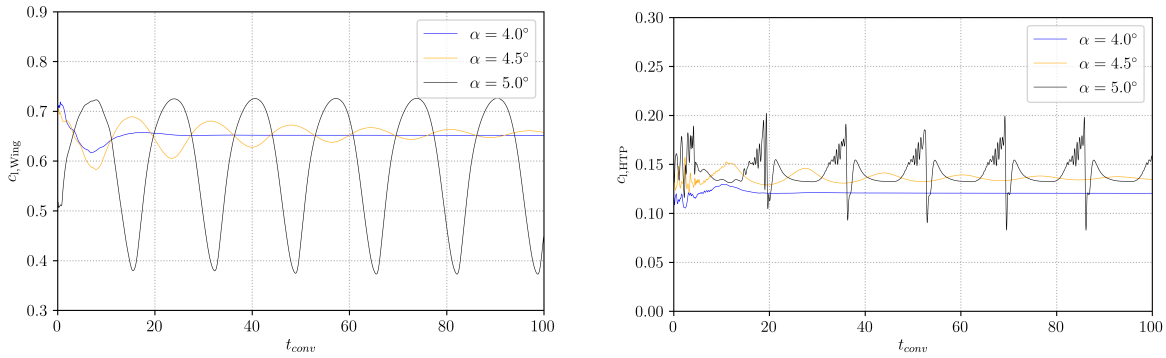

(a) Wing (b) HTP

Figure 13: Lift coefficient time series of the wing (left) and HTP (right) components for a variation of the angle of attack at $M = 0.6963$

The time signals for $\alpha = 5.0°$ and the corresponding spectral densities are shown in Fig. 14 and 15. The periodic low frequency oscillation of the wing lift coefficient is related to transonic shock buffet. A dominant frequency can be identified at $Sr \approx 0.06$. This is in good agreement to the buffet onset frequency experimentally observed by Jacquin et al. [25] on a different supercritical airfoil. The area filled in blue indicates the range of typical buffet onset frequencies [25].

The peaks due to shock buffet on the wing section are also present in the lift signal of the HTP section (see Fig. 15). However, higher frequencies contribute to the PSD spectra with a dominant peak at $Sr \approx 2.5$. This frequency is located in the range of vortex shedding frequencies reported by Huang and Lin [24], which is indicated by the area filled in red. Both, the low and high frequency peaks were also observed in a similar range by a numerical analysis based on hybrid RANS/LES simulations by Kleinert et al. [3] for a different configuration and flow conditions.

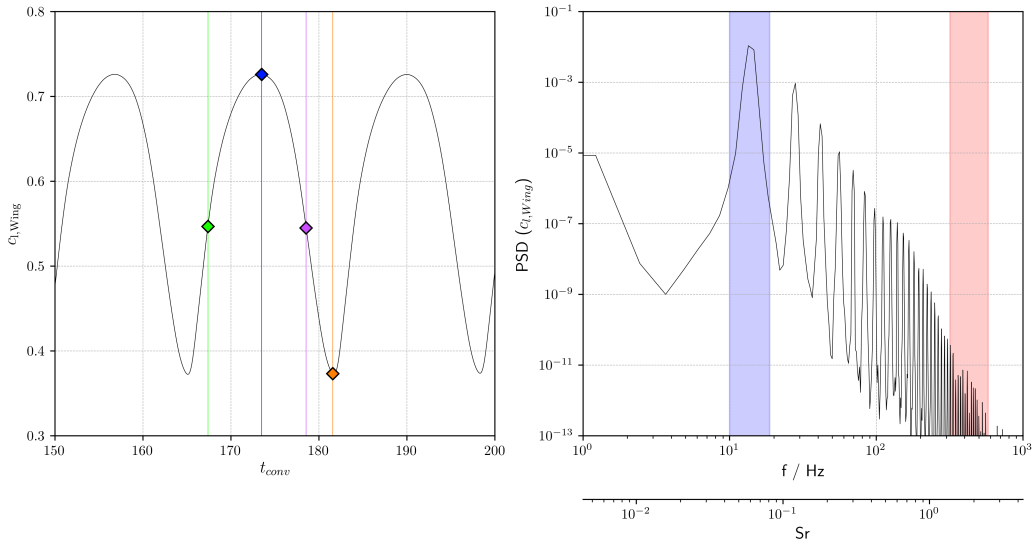

Figure 14: Time signal of the lift coefficient (left) and power spectral densities (right) of the wing section at $M = 0.6963$ and $\alpha = 5.0°$

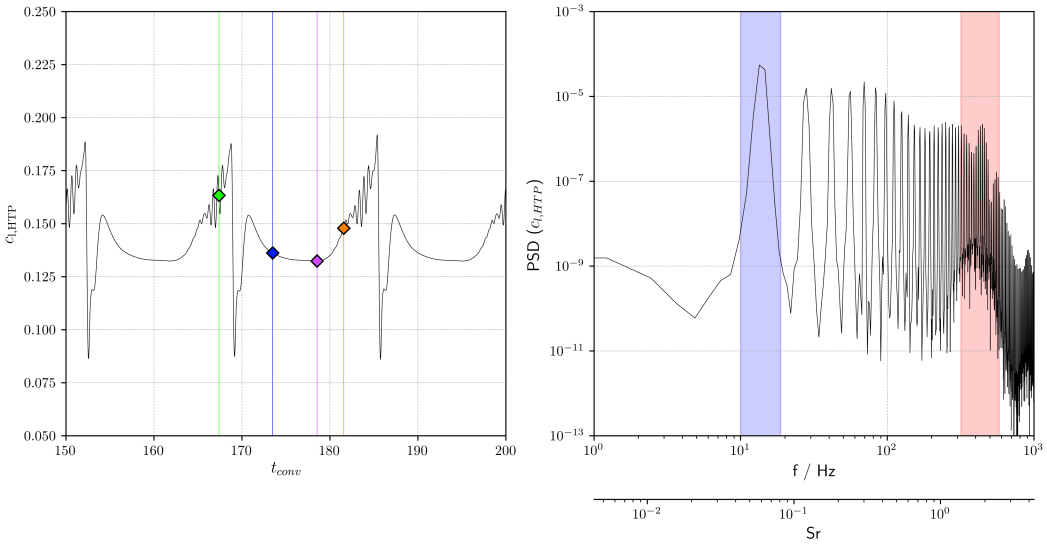

Figure 15: Time signal of the lift coefficient (left) and power spectral densities (right) of the HTP section at $M = 0.6963$ and $\alpha = 5.0°$

Similar to the low speed case, the development of the flow field is discussed over one buffet cycle for the times marked in Fig. 14 and 15. Again, the pressure and skin friction distributions, as well as the vorticity fields are consulted in Fig. 16 and 17, respectively. At the first snapshot (green symbol, $t_{conv} = 167.4$), the lift of the wing section increases due to a downstream movement of the shock. The boundary layer remains attached and the shear layer is stable. In contrast, the HTP is located in a region of vortical structures which were produced in a previous time step, causing the high frequency oscillations in the lift coefficient (see Fig. 15). At the time where the maximum lift coefficient is present on the wing section (blue symbol, $t_{conv} = 173.5$), the shock is located at the most downstream location ($x/c \approx 0.38$), with a region of shock induced separation up to $x/c \approx 0.6$. During this time, the shear layer and the wake are only extended weakly normal to the main flow direction without the presence of vortical structures.

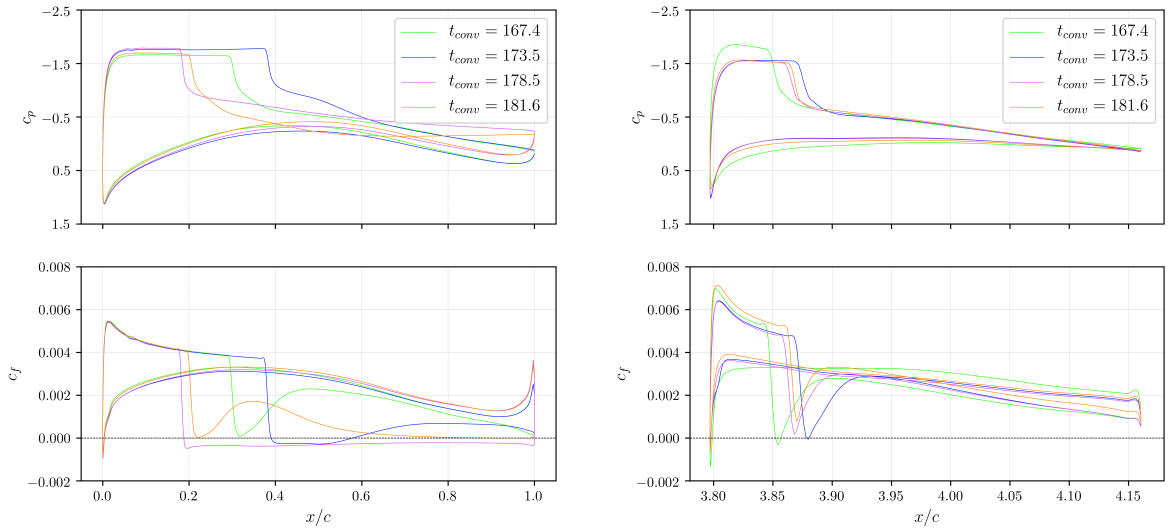

(a) Wing (b) HTP

Figure 16: Instantaneous pressure and skin friction distributions on the wing and HTP sections at $M = 0.6963$ and $\alpha = 5.0°$

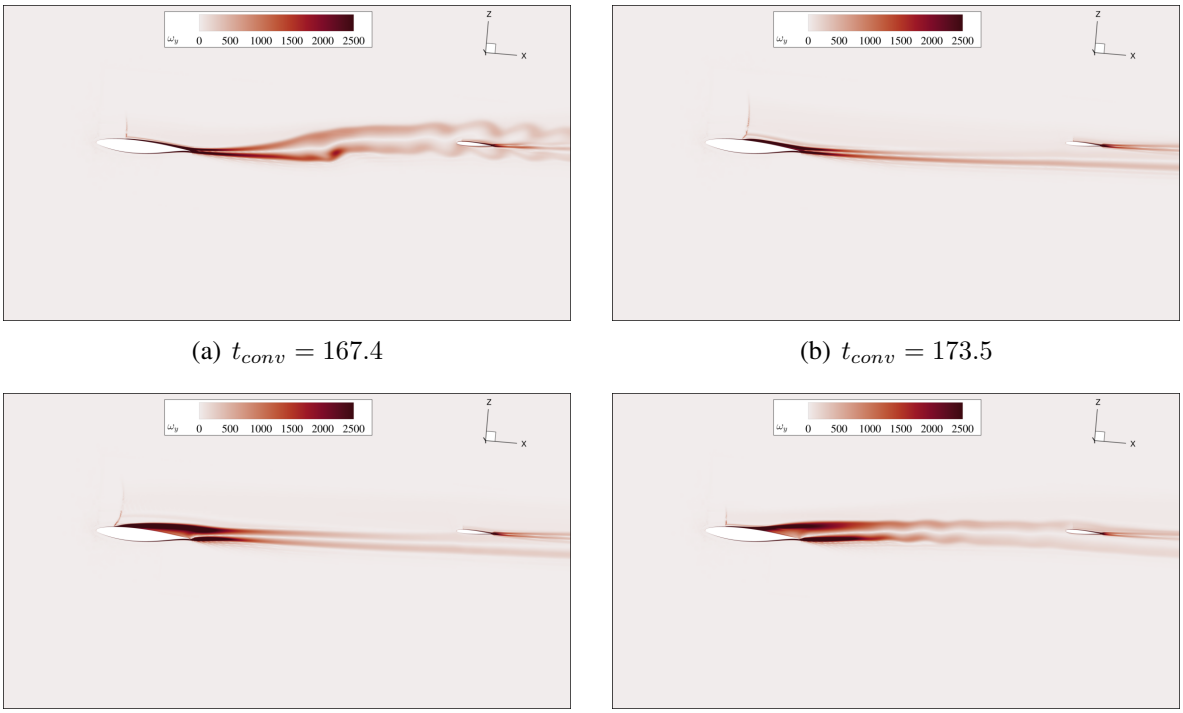

(a) $t_{conv} = 167.4$ (b) $t_{conv} = 173.5$

(c) $t_{conv} = 178.5$ (d) $t_{conv} = 181.6$

Figure 17: Instantaneous vorticity at $M = 0.6963$ and $\alpha = 5.0°$

In particular, the wake convects beneath the HTP. During the lift breakdown of the wing section (magenta symbol, $t_{conv} = 178.5$), the shock is moving towards the leading edge. The boundary layer is separated downstream of the shock location up to the trailing edge, leading to a widening of the shear layer on the upper wing section. Eventually, the vortex shedding process is initiated, which is already present in the first snapshot (see Fig. 17).

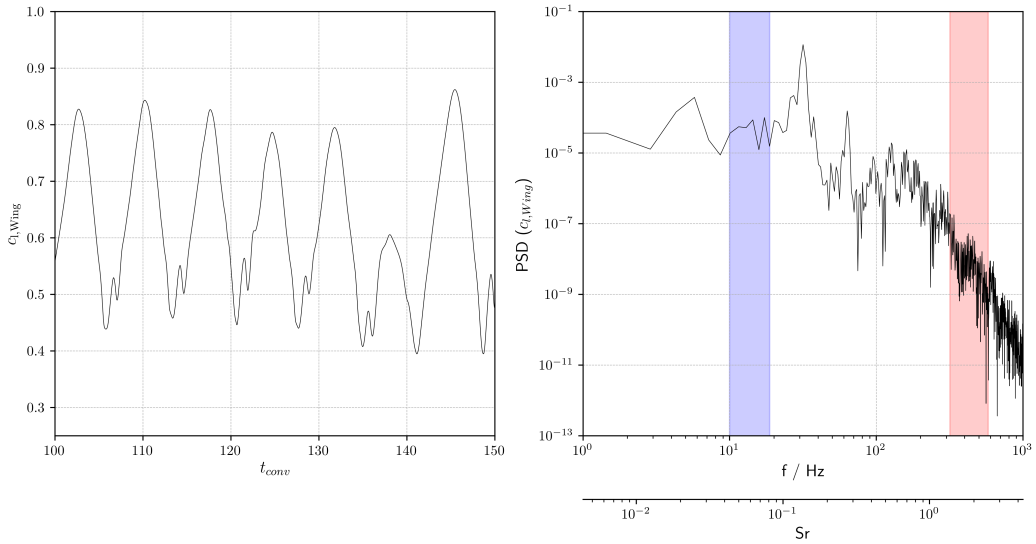

Figure 18: Time signal of the lift coefficient (left) and power spectral densities (right) of the wing section at $M = 0.6963$ and $\alpha = 8.0°$

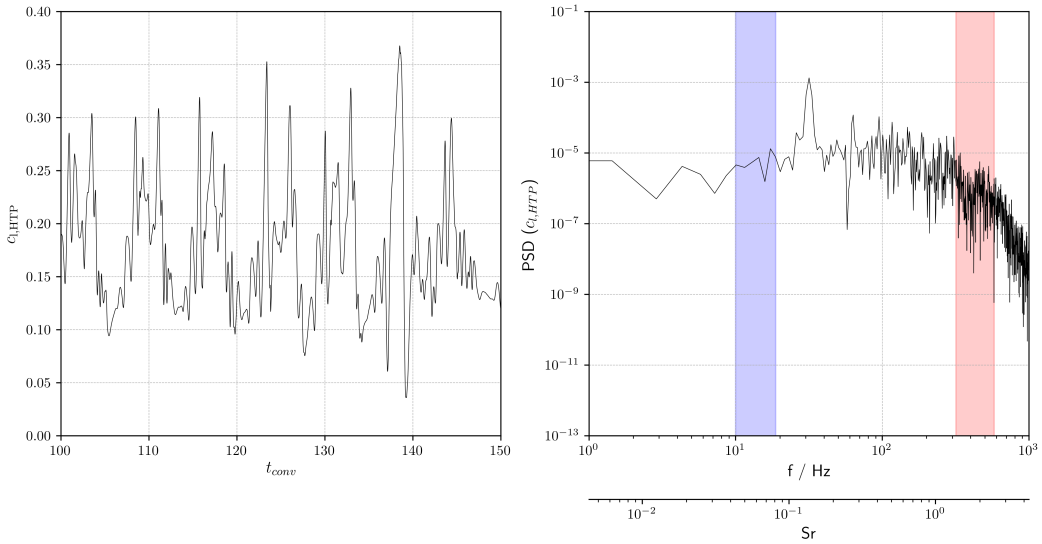

Figure 19: Time signal of the lift coefficient (left) and power spectral densities (right) of the HTP section at $M = 0.6963$ and $\alpha = 8.0°$

The effect of an increase of the angle of the angle of attack is discussed for $\alpha = 8.0°$. As indicated in the steady polar (see Fig. 4), this angle of attack is located in the deep stall region. The time series of the lift coefficient for the wing and HTP sections shown in Fig. 18 and 19 suggest a less periodic character as compared to the buffet onset case at $\alpha = 5.0°$. Furthermore, the shock buffet frequency is increased to a frequency of $f = 30$ Hz, or a Strouhal number of $Sr = 0.15$. This peak is also dominant at the HTP section, however, the spectrum appears to be distributed in a broadband sense compared to the buffet onset condition.

Fig. 20 provides an insight into the flow field based on instantaneous snapshots for the vorticity and Mach number, suggesting that a substantial more intense vortex shedding is dominating compared to the buffet onset case $\alpha = 5.0°$. As listed in Tab. 3, the fluctuations on the HTP section are strongly increased for $\alpha = 8.0°$ compared to $\alpha = 5.0°$. However, the highest fluctuations are present for the low speed case at $\alpha = 19.0°$, where the $c_{l,rms,HTP}$ values are more than twice as high compared to the high speed case at $\alpha = 8.0°$.

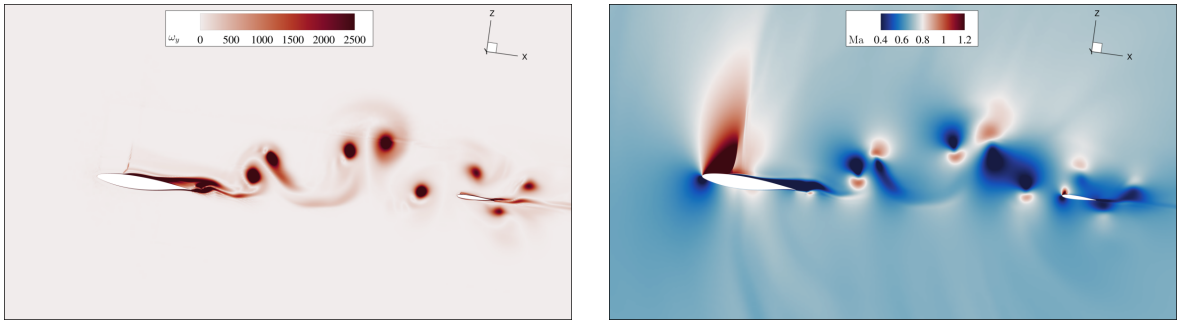

(a) Vorticity (b) Mach number

Figure 20: Instantaneous vorticity at $M = 0.6963$ and $\alpha = 8.0°$

Table 3: Fluctuations of the lift coefficient for high speed buffet onset and deep stall conditions

α	$c_{l,rms,Wing}$	$c_{l,rms,HTP}$
5.0	0.1193	0.0150
8.0	0.1277	0.0572

4 CONCLUSIONS

This paper presents a numerical study of the unsteady interaction between a wing and an HTP in 2D flows based on unsteady RANS simulations. The investigated configuration is derived from the NASA Common Research model at a constant spanwise position. Steady simulations are performed for low speed and high speed flows to locate the appearance of first unsteadinesses in the flow field, followed by unsteady simulations for a selected range of the angle of attack. HTP buffet cases in the sense of an unsteady inflow causing fluctuations on the surface of the HTP are identified for both, low speed and high speed flows.

The appearance of fluctuations on the HTP is found to be strongly depending on the boundary layer state of the main wing section. In general, a distinct separation causes the formation of large vortical structures, which convect towards the HTP and eventually cause high fluctuations. In contrast, a temporary attached boundary layer leads to a comparatively thin wake and thus to an almost undisturbed inflow of the HTP.

At the corresponding buffet onset condition, a dominant low frequency oscillation is present at a Strouhal number of $Sr = 0.11$ for the low speed case and $Sr = 0.06$ for the high speed

case. For the low speed case, this frequency is in agreement to the stall onset of airfoils with a combination of thin airfoil and trailing edge stall types. The frequency of $Sr = 0.06$ for the high speed case is in agreement to the shock buffet onset frequency of supercritical airfoils. Further frequency content in the typical range of vortex shedding is identified, which becomes dominant for the low speed case at high angles of attack. Furthermore, the fluctuations on the HTP are distributed in a broadband sense with increasing amplitudes in deep stall conditions. This is true for low speed and high speed flows. The highest fluctuations are present at low speed conditions. In order to assess the effect of the corresponding flow mechanisms on an elastic structure (buffeting), further studies are required based on coupled fluid-structure simulations.

5 REFERENCES

[1] Koopmans, W., Klabes, A., Gojny, M. H. (2022). Wing-Tailplane Flow Interaction: Flight Test Data Analysis From Stall Flights. In: *Proceedings International Forum on Aeroelasticity and Structural Dynamics (IFASD)*, Madrid.

[2] Thomspon, D. (1997). Effect of the Leading-Edge Extension (LES) Fence on the Vortex Structure over the F/A-18, Technical Report DSTO-TR-0489, DSTO.

[3] Kleinert, J., Stober, J., Lutz, T. (2023): Numerical simulation of wake interactions on a tandem wing configuration in high-speed stall conditions. *CEAS Aeronautical Journal*, 14, 171-186.

[4] Waldmann, A., Konrath, R., Lutz, T., and Krämer, E. (2020). Unsteady Wake and Tailplane Loads of the Common Research Model in Low Speed Stall. In: *New Results in Numerical and Experimental Fluid Mechanics XII*, edited by A. Dillmann, G. Heller, E. Krämer, C. Wagner, C. Tropea, and S. Jakirlic, *Notes on Numerical Fluid Mechanics and Multidisciplinary Design*, Vol. 142, Springer, Cham, Switzerland.

[5] Lutz, T., Kleinert, J., Waldmann, A., Koop, L., Yorita, D., Dietz, G. and Schulz, M. (2023). Research Initiative for Numerical and Experimental Studies on High-Speed Stall of Civil Aircraft. *Journal of Aircraft*, 60(3), 623-636.

[6] Davies, K. (2023). Unsteady RANS simulations of two dimensional separated wake flows. In: Proceedings of the 21st STAB-Workshop 2023 in Göttingen.

[7] Vassberg, J. C., DeHaan, M. A., Rivers, S. M., Wahls, R. A. (2008). Development of a Common Research Model for Applied CFD Validation Studies, AIAA Paper 2008-6919.

[8] Vassberg, J. C., DeHaan, M. A., Rivers, S. M., Wahls, R. A. (2018). Retrospective on the Common Research Model for Computational Fluid Dynamics Validation Studies. *Journal of Aircraft*, 55(4), 1325-1337.

[9] CentaurSoft (2024). CENTAUR Grid Generator. *https://home.centaursoft.com/*. Accessed: 2024-05-28.

[10] Wunderlich, T. F. (2013). Multidisziplinäre Optimierung von Flügeln für Verkehrsflugzeuge mit Berücksichtigung der statischen Aeroelastizität. PhD thesis, Technische Universität Braunschweig.

[11] Keller, D. (2017). High-Lift Design for a Forward Swept Natural Laminar Flow Wing. *CEAS Aeronautical Journal*, 11, 81-92.

[12] Schwamborn, D., Gerhold, T., Heinrich, R. (2006). The DLR TAU-Code: Recent Applications in Research and Industry. In: *Proceedings European Conference on Computational Fluid Dynamics ECCOMAS*, TU Delft, Delft.

[13] Dwight, R. (2006). Efficiency Improvements of RANS-Based Analysis and Optimization using Implicit and Adjoint Methods on Unstructured Grids. PhD thesis, University of Manchester.

[14] Jameson, A. (1991). Time dependent calculations using multigrid, with applications to unsteady flows past airfoils and wings. 10th Computational Fluid Dynamics Conference, AIAA, 91-1596, Honolulu

[15] Eisfeld, B., and Brodersen, O. (2005). Advanced Turbulence Modelling and Stress Analysis for the DLR-F6 Configuration. AIAA Paper 2005-4727.

[16] Speziale, C. G., Sarkar, S. and Gatski, T. B. (1991). Modelling the Pressure-Strain Correlation of Turbulence: An Invariant Dynamical Systems Approach. *Journal of Fluid Mechanics*, 227, 245-272.

[17] Launder, B. E., Reece, G. J. and Rodi, W. (1975). Computations of Complex Flow Configurations Using a Modified Elliptic-Blending Reynolds-Stress Model. *Journal of Fluid Mechanics*, 68(3), 537-566.

[18] Menter, F. R. (1994). Two-Equation Eddy-Viscosity Turbulence Models for Engineering Applications. *AIAA Journal*, 32(8), 1598-1605.

[19] Eisfeld, B., Rumsey C.L., Togiti, V., Braun, S. and Stürmer, A. (2022). Reynolds-Stress Model Computations of NASA Juncture Flow Experiment. *AIAA Journal*, 60(3), 1643-1662.

[20] P. Welch (1967). The use of the fast Fourier transform for the estimation of power spectra: A method based on time averaging over short, modified periodograms. *IEEE Trans. Audio Electroacoust*, 15, 70-73.

[21] Zaman, K.B.M.Q., McKinzie, D.J. and Rumsey, C.L. (1989). A Natural Low-Frequency Oscillation Over Airfoils Near Stalling Conditions. *Journal of Fluid Mechanics*, 202, 403-442.

[22] Broeren, A.B. and Bragg, M.B. (1998). Low-Frequency Flowfield Unsteadiness During Airfoil Stall and the Influence of Stall Type. In: 16^{th} AIAA Applied Aerodynamics Conference, AIAA 1998-2571, Albuquerque.

[23] Roshko, A. (1954). On the Drag and Shedding Frequency of Two-Dimensional Bluff Bodies. NACA TN-3169.

[24] Huang, R. F., and Lin, C. L., (1995). Vortex Shedding and Shear-Layer Instability of Wing at Low-Reynolds Numbers. *AIAA Journal*, 33(8), 1398–1403.

[25] Jacquin, L., Molton, P., Deck, S., Maury, B. and Soulevant, D.(2009). Experimental Study of Shock Oscillation over a Transonic Supercritical Profile. *AIAA Journal*, 47(9), 1985–2270.

COPYRIGHT STATEMENT